IEEE Access
Multidisciplinary | Rapid Review | Open Access Journal

Received February 9, 2022, accepted February 25, 2022, date of publication March 8, 2022, date of current version March 15, 2022.

Digital Object Identifier 10.1109/ACCESS.2022.3157610

Control of Haptic Systems Based on Input-to-State Stability

SUYONG KIM AND DOO YONG LEE, (Senior Member, IEEE)
Department of Mechanical Engineering, Korea Advanced Institute of Science and Technology, Daejeon 34141, South Korea

Corresponding author: Doo Yong Lee (leedy@kaist.ac.kr)

This work was supported in part by the National Research Foundation of Korea (NRF) Grant funded by the Korea Government [Ministry of Science and ICT (MSIT)] under Grant 1711111113; and in part by the Brain Korea 21 Plus Program, in 2021.

ABSTRACT Discretization of signals often generates additional energy in the haptic systems, and makes them unstable. The currently popular controls based on the passivity stabilize the systems by limiting the rendered force of the haptic systems so that the generated energy from the system stays below zero. The passivity-based methods are, however, often conservative and sacrifice the performance of haptic rendering. This paper proposes a control method to adjust the change rate of the stiffness of virtual environment connected to the haptic systems to satisfy the input-to-state stability (ISS) for better stability and transparency. The ISS conditions for the systems are derived by modeling the system as a linear time-varying system. The systems become dissipative if they satisfy the ISS conditions. The generated surplus energy of the dissipative system is less than a positive finite value while maintaining stability. Since the passive system is a special case of the dissipative system, the proposed ISS-based control is less conservative than the passivity-based approaches. Performance of the proposed control is experimentally compared with the virtual coupling and the force-bounding method that are widely used passivity-based approaches. The energy generated from the system using the proposed method is positive finite whereas the generated energy using the passivity-based approaches is less than zero. This means that more energy is transferred to the operator. Increased stiffness corresponding to this additionally transferred energy can be rendered. Root-mean-square and maximum errors of the rendered forces are, therefore, reduced by at least 86 % and 50 %, respectively.

INDEX TERMS Haptic interface, haptic rendering, virtual simulation, input-to-state stability.

I. INTRODUCTION

Virtual environment connected to haptic systems may behave active due to signal discretization by the sampler, zero-order hold (ZOH), and velocity estimation [1], [2]. This active behavior incurs additional energy in the system and makes it unstable. The discretization effect becomes worse as the stiffness of the virtual environment and sampling time increase. Physics-based simulations involving deformable objects have slow force update rate of 300 Hz to 500 Hz due to large amounts of computation [3], which increases the active behavior of the haptic systems. It is important to enhance transparency while maintaining stability in systems that require high-fidelity haptic feedback, such as medical simulations.

Time-domain passivity approach (TDPA) stabilizes the systems by observing and controlling the energy additionally generated by the systems. Hannaford and Ryu [4] proposed a passivity observer and controller to preserve the system passivity. The passivity observer monitors the system energy in real-time, and excessive energy generated by the system is dissipated by the artificial damping force called the passivity controller. There are studies to improve the transparency of TDPA by predicting the system energy and reducing the observed energy [5]. The operator, however, may feel discrete feedback force because the controller works discontinuously depending on the observer state. The discontinuous feedback force sometimes causes contact oscillations especially when the haptic device is moving at a low velocity [6]. There is a possibility that the observer may not detect unstable motion even if the system diverges due to the accumulated energy even in a stable environment and free space. This is called a memory effect, and it becomes worse in the environment where soft and stiff objects are mixed [7].

Output-limiting methods such as adjusting output-limiter [8] and force-bounding approach (FBA) [9]–[11] have

The associate editor coordinating the review of this manuscript and approving it for publication was Haibin Sun.

been reported to limit the maximum environment force to guarantee the passivity of the system. These methods are free of discontinuous feedback force unlike TDPA since they limit the rendered force. The haptic system is modeled as a one or two-port network, and the maximum environment force is computed based on the TDPA. The environment force is transmitted faithfully if it is less than the computed maximum force. The memory effect, however, occurs as in the TDPA since the system energy is observed in the time domain. A more conservative condition from scaling down the device damping [9] is used to handle the memory effect, thereby, deteriorating the transparency more than necessary.

There have been many researches to stabilize the haptic systems by limiting the environment impedance. Colgate *et al.* [12] proposed the virtual coupling that connects the device and the virtual tool with a spring and a damper. The haptic systems are modeled as a two-port network, and the spring and damper of the virtual coupling are designed to satisfy the passivity of the systems [13], [14]. The virtual coupling limits the environment impedance, and keeps the system passive. The virtual coupling is used in a wide range of applications including real-time simulation with deformable objects [15]–[17]. There is a disadvantage that the transparency of haptic rendering is degraded by the virtual coupling. The operator always feels a softer environment than the original environment since the spring of the virtual coupling is connected to the environment in series.

Methods to improve the transparency have been proposed. The input-output coupling method [18]–[20] keeps the system dissipative by controlling the coupled terms to satisfy the input-to-state stability (ISS) condition. These methods analyze the ISS considering hysteresis of the input-output [21], and control the input-output by coupling derivatives of the input-output pairs. The coupled pairs are controlled to satisfy the constraint expressed as the function of the derivatives pairs and the maximum slope of the hysteresis. The energy generated in the system is bounded to a finite value, and the system remains dissipative. Maximum renderable stiffness is increased compared to the previous control methods using the passivity. Haptic fidelity, however, deteriorates because bounded vibration may be included in the rendered force. Additional damping force, manually tuned by the operator, is required to prevent the vibration. This damping must be re-adjusted experimentally for the new environment or operator. Model matching framework has been proposed to render the stiff environment [6]. The controller is designed based on the H_∞ optimization problem to minimize the error between the rendered force and the desired force. Accurate knowledge of the physical properties of the environment is necessary to design the controller. Singh *et al.* [22], [23] proposed successive force augmentation (SFA) approach to improve transparency by adding an offset force to the force generated by the virtual coupling. The offset force is updated successively according to the pressing path and the target stiffness of the environment. This method depends on accurate knowledge of the physical properties of the environment.

Previous control methods based on the passivity condition, that limit the rendered force or impedance of the environment or simulation, achieve the goal of stabilization by keeping the energy generated from the environment less than zero. These approaches often lead to conservative control, and sacrifice the performance of haptic rendering. The previous methods developed to enhance the transparency of the haptic rendering, such as the input-output coupling method, model matching framework, and SFA approach, require accurate models and knowledge of the environment physics.

This paper proposes a control method that adjusts the change rate of the stiffness of the virtual environment to satisfy the input-to-state stability (ISS) conditions to enhance the transparency without a priori accurate model of knowledge of the environment physics. The nonlinear environment is modeled as a linear time-varying spring k_{dis}. The characteristics of the nonlinear environment are included since k_{dis} is calculated at each time step. The ISS conditions for the haptic systems are derived by modeling the system as a linear time-varying system. The change rate of k_{dis} is monitored at each time step, and it is adjusted to satisfy the ISS conditions. The haptic systems become dissipative if they satisfy the ISS condition [24]. The generated surplus energy of the dissipative system is less than a positive finite value [18]. The passive system is a special case of the dissipative system, where the generated energy is strictly less than zero. The proposed ISS-based control keeps the system dissipative, and the rendered force is controlled so that the generated energy has a positive finite value as long as stability is maintained. More energy of the system using the proposed controller, compared to the system with the passivity-based approaches, can be transmitted to the operator. Hence increased stiffness of the environment corresponding to the surplus energy can be rendered to the operator. This means that the fidelity of the haptic system is improved. The proposed control uses only the current magnitudes of the position of the haptic device and the environment force, and it does not require any exact model of the environment. Experiment results to compare the performance of the haptic rendering of the proposed method with the previous virtual coupling and FBA methods show improved fidelity of the rendered force while maintaining the stability.

Modeling of the haptic systems as the linear time-varying systems is explained in Section II. The ISS conditions for the haptic systems are derived in Section III. Control design based on the ISS conditions to stabilize the systems is presented in Section IV-A. Control design to enhance the rendering performance is presented in Section IV-B. Experimental comparison with the passivity-based approaches is explained in Section V.

II. SYSTEM MODEL

The displayed stiffness $k_{dis}(n)$ felt by the operator at n^{th} time step is computed as the environment force $F_e(n)$ divided by the penetration depth $x_h(n)$ of the virtual tool from the

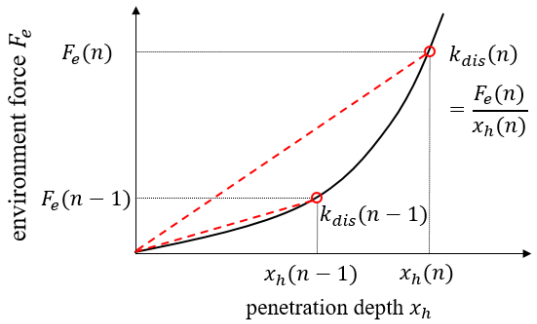

FIGURE 1. Linear time-varying spring $k_{dis}(n)$ to represent the nonlinear environment.

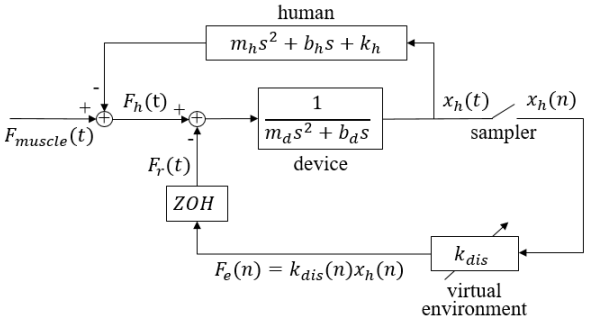

FIGURE 2. Haptic systems with discretized signals.

environment surface as shown in (1) and Fig. 1.

$$k_{dis}(n) = \frac{F_e(n)}{x_h(n)}. \tag{1}$$

Fig. 2 shows a typical model of the haptic systems including the operator, device and virtual environment with discretized and quantized signals. Muscle force $F_{muscle}(t)$ is generated by the operator's intention. Contact force $F_h(t)$ generated by the operator and position $x_h(t)$ are transmitted to the haptic device. $F_h(t)$ is bounded. $x_h(t)$ is discretized into $x_h(n)$ by the sampler. The device is modeled as mass m_d and damping b_d. $F_e(n) = k_{dis}(n)x_h(n)$ is generated by the virtual environment. $F_e(n)$ turns into analog signal $F_r(t) = F_e(n)ZOH$ which is the force rendered to the operator. Physics-based simulations involving deformable objects have slow force update rates of 300 Hz to 500 Hz due to large amounts of computation [3]. Sampling time T is assumed to be 2 ms in this paper for the sake of analysis, which is considered typical and plausible in haptic systems. The proposed method can be also applied to systems with sampling times of less than 2 ms for stiffer envirionments. Physical damping of the passive human operator improves stability [25], [26]. Stability condition without the operator's impedance is, therefore, more conservative than ensuring the stability with human operator, which is adapted in this paper to show merits of the proposed method.

Fig. 3 (a) shows the haptic systems excluding the operator impedance. Fig. 3 (b) shows the equivalent system in the continuous-time domain. The sampler and ZOH is given in [27]. The e^{-sT} is replaced with Taylor series as in (3).

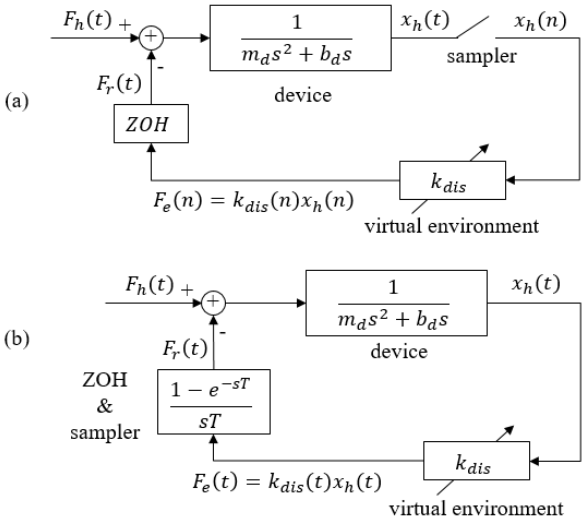

FIGURE 3. (a) Haptic systems excluding the operator impedance; (b) Equivalence in the continuous-time domain.

It is known that the human operator applies a position input of up to 20 Hz in typical haptic rendering [7]. The terms of third or higher order in the Taylor series (3) are assumed negligible considering the maximum frequency of 20 Hz is small compared to the sampling frequency, 500 Hz. Hence, the sampler and ZOH are modeled as in (4).

$$ZOH(s)sample(s) = \frac{1 - e^{-sT}}{sT}. \tag{2}$$

$$e^{-sT} = 1 - sT + \frac{(-sT)^2}{2!} + \cdots. \tag{3}$$

$$\begin{aligned} ZOH(s)sample(s) &\cong \frac{1 - (1 - sT + \frac{(-sT)^2}{2!})}{sT} \\ &= 1 - \frac{T}{2}s. \end{aligned} \tag{4}$$

Equation (5) shows $F_r(t) = F_e(n)ZOH$. $F_e(t)$ is the environment force in the continuous-time domain as shown in Fig. 3 (b). $F_e(t)$ is the same as $k_{dis}(t)x_h(t)$. The $k_{dis}(t)$ is the displayed stiffness of the environment at time t. $F_e(s)$ is Laplace transformation of $F_e(t)$. $F_e(n)ZOH$ is equivalent to the inverse Laplace transform of $F_e(s)\frac{1-e^{-sT}}{sT}$ and approximated as the inverse Laplace transform of $F_e(s)\left(1 - \frac{T}{2}s\right)$ by using (4). Hence $F_r(t)$ is expressed as a function of $k_{dis}(t)$, $x_h(t)$ and T.

$$\begin{aligned} F_r(t) &= F_e(n)ZOH = \mathcal{L}^{-1}\left\{F_e(s)\frac{1 - e^{-sT}}{sT}\right\} \\ &\cong \mathcal{L}^{-1}\left\{F_e(s)\left(1 - \frac{T}{2}s\right)\right\} = F_e(t) - \frac{T}{2}\frac{d}{dt}(F_e(t)) \\ &= k_{dis}(t)x_h(t) - \frac{T}{2}\frac{d}{dt}(k_{dis}(t)x_h(t)) \\ &= \left\{k_{dis}(t) - \frac{T}{2}\dot{k}_{dis}(t)\right\}x_h(t) - \frac{T}{2}k_{dis}(t)\dot{x}_h(t). \end{aligned} \tag{5}$$

An ideal $F_r(t)$ is the same as $k_{dis}(t)x_h(t)$. $F_r(t)$ under the effect of the discretization becomes $k_{dis}(t)x_h(t)$ with

additional terms, $-\frac{T}{2}k_{dis}(t)\dot{x_h}(t)$ and $-\frac{T}{2}\dot{k}_{dis}(t)x_h(t)$ as in (5), resulting in unintended force of damping and spring.

Differential equation of the system is shown in (6). The unintended negative damping, $-\frac{T}{2}k_{dis}(t)$ and spring, $-\frac{T}{2}\dot{k}_{dis}(t)$ occur due to the discretization effect. Hence the effective damping $b_{eff}(t)$ and spring $k_{eff}(t)$ of the system become $b_d - \frac{T}{2}k_{dis}(t)$ and $k_{dis}(t) - \frac{T}{2}\dot{k}_{dis}(t)$, respectively. The haptic system is expressed as a linear time-varying system where $b_{eff}(t)$ and $k_{eff}(t)$ vary according to $k_{dis}(t)$ and T.

$$\begin{aligned} F_h(t) &= m_d\ddot{x_h}(t) + b_d\dot{x_h}(t) + F_r(t) \\ &\cong m_d\ddot{x_h}(t) + \left\{b_d - \frac{T}{2}k_{dis}(t)\right\}\dot{x_h}(t) \\ &\quad + \left\{k_{dis}(t) - \frac{T}{2}\dot{k}_{dis}(t)\right\}x_h(t) \\ &= m_d(t)\ddot{x_h}(t) + b_{eff}(t)\dot{x_h}(t) + k_{eff}(t)x_h(t), \end{aligned} \tag{6}$$

where $b_{eff}(t)$ and $k_{eff}(t)$ denote $b_d - \frac{T}{2}k_{dis}(t)$ and $k_{dis}(t) - \frac{T}{2}\dot{k}_{dis}(t)$, respectively.

III. INPUT-TO-STATE STABILITY CONDITIONS

Conditions for the system to satisfy the ISS are derived in this section. The haptic system is dissipative if it is ISS [24]. Equation (7) shows the energy stored in. the system. The generated surplus energy of the dissipative system is less than a positive finite value α as shown in (7) [18]. The passive system is a special case of the dissipative system, where the generated energy is strictly less than zero, i.e., α in (7) is zero. The proposed ISS-based control in section IV keeps the system dissipative, and the rendered force is controlled so that the generated energy has a positive finite value. More energy generated in the dissipative system compared to the passive system is transmitted to the operator. Increased stiffness of the environment corresponding to the surplus energy can be rendered to the operator while maintaining the stability of the system. The ISS is, therefore, less conservative than the passivity, and the fidelity of haptic rendering is improved using the ISS-based control.

Theorem 1[24]: The system is dissipative if and only if the system is ISS.

$$\int_o^T F_r(t)\dot{x_h}(t) \geq -\alpha, \quad \textit{where } \alpha < \infty. \tag{7}$$

The ISS conditions is applied to the linear time-varying system (6). Four conditions to satisfy ISS are derived. Consider the following system,

$$\dot{x} = f(x, F), \tag{8}$$

where $x \in \mathbb{R}^n$ and F $\in \mathbb{R}^m$ are the state and input, respectively. $f : \mathbb{R}^n \times \mathbb{R}^m$ is assumed as locally Lipschitz function $f(0, 0) = 0$.

Theorem 2 [24]: The system in (8) is ISS if and only if there exists a positive definite and proper ISS-Lyapunov function $V : \mathbb{R}^n \to \mathbb{R}$ such that the following inequality is satisfied.

$$\dot{V}(x, F) \leq -\beta(|x|) + \gamma(|F|), \tag{9}$$

where β and γ belong to a class $\mathcal{K}_\infty$ function. |.| denotes Euclidean norm.

An ISS-Lyapunov function candidate is designed as in (10).

$$V = \frac{1}{2}m_d(x_2 + x_1)^2 + \frac{1}{2}(k_{dis} + b_{eff})x_1^2 > 0, \tag{10}$$

where $x_1 = x_h(t)$, $x_2 = \dot{x}_h(t)$, $b_{eff} = b_{eff}(t)$ and $k_{dis} = k_{dis}(t)$. $\left(k_{dis} + b_{eff}\right)$ in (10) should be positive definite for V to be positive definite. The other terms are positive definite. Condition I for the system to be ISS is as follows.

$$\text{Condition I} : k_{dis} + b_{eff} > 0. \tag{11}$$

Time derivative of the ISS-Lyapunov function candidate is as follows.

$$\begin{aligned} \dot{V} &= \{m_d(x_2 + x_1)x_3 + m_d(x_2 + x_1)x_2\} \\ &\quad + \left\{\frac{1}{2}\left(\dot{k}_{dis} + \dot{b}_{eff}\right)x_1^2 + (k_{dis} + b_{eff})x_1x_2\right\}, \end{aligned} \tag{12}$$

where $x_3 = \ddot{x}_h(t)$.

The m_dx_3 is the same as $(F - b_{eff}x_2 - k_{eff}x_1)$ according to (6). Equation (12) is rearranged as follows.

$$\begin{aligned} \dot{V} &= \left\{(x_2 + x_1)\left(F - b_{eff}x_2 - k_{eff}x_1\right) + m_d(x_2 + x_1)x_2\right\} \\ &\quad + \left\{\frac{1}{2}\left(\dot{k}_{dis} + \dot{b}_{eff}\right)x_1^2 + (k_{dis} + b_{eff})x_1x_2\right\} \\ &= -\left(b_{eff} - m_d\right)x_2^2 \\ &\quad + \left\{F + \left(m_d - k_{eff} + k_{dis}\right)x_1\right\}x_2 \\ &\quad - \left(k_{eff} - \frac{1}{2}\dot{k}_{dis} - \frac{1}{2}\dot{b}_{eff}\right)x_1^2 + Fx_1 \\ &= -Ax_2^2 + Bx_2 - Cx_1^2 + Fx_1, \end{aligned} \tag{13}$$

where $A = b_{eff} - m_d$, $B = F + (m_d - k_{eff} + k_{dis})x_1$, $C = k_{eff} - \frac{1}{2}\dot{k}_{dis} - \frac{1}{2}\dot{b}_{eff}$.

The A, B, and C in (13) represent the coefficients of $-x_2^2$, x_2, and $-{x_1}^2$, respectively. The A should be positive definite to satisfy the ISS condition (9) since it is a coefficient of $-x_2^2$. This is the condition II as in (14). $Bx_2 - Cx_1^2 + Fx_1$ in (13) is expressed as inequalities in (15) to (19).

$$\text{condition II} : A = b_{eff} - m_d > 0. \tag{14}$$

The inequality (15) holds for $-Ax_2^2 + Bx_2$ in (13) since $A > 0$. The inequality (16) is obtained by substituting (15) into (13).

$$\begin{aligned} &-Ax_2^2 + Bx_2 \\ &\quad = -\frac{1}{2}Ax_2^2 - \left(\frac{1}{2}Ax_2^2 - Bx_2 + \frac{1}{2A}B^2\right) + \frac{1}{2A}B^2 \\ &\quad = -\frac{1}{2}Ax_2^2 - \frac{1}{2}A\left(x_2 - \frac{B}{A}\right)^2 + \frac{1}{2A}B^2 \\ &\quad \leq -\frac{1}{2}Ax_2^2 + \frac{1}{2A}B^2. \end{aligned} \tag{15}$$

$$\dot{V} \leq -\frac{1}{2}Ax_2^2 + \frac{1}{2A}B^2 - Cx_1^2 + Fx_1. \tag{16}$$

TABLE 1. Conditions for ISS.

Condition	Function
I	$k_{dis} + b_{eff} > 0$
II	$A = b_{eff} - m_d > 0$
III	$-\frac{1+D^2}{2A} + C - \frac{1}{2} > 0$ where $C = k_{eff} - \frac{1}{2}\dot{k}_{dis} - \frac{1}{2}\dot{b}_{eff}$, $D = m_d - k_{eff} + k_{dis}$.
IV	$\frac{1+D^2}{2A} + \frac{1}{2} > 0$

The D denotes $m_d - k_{eff} + k_{dis}$ of B. B^2 in (16) satisfies the inequality (17)

$$\begin{aligned} B^2 &= (F + Dx_1)^2 = F^2 + 2DFx_1 + D^2x_1^2 \\ &\le F^2 + \left\{(DF)^2 + x_1^2\right\} + D^2x_1^2 \\ &= \left(1 + D^2\right)\left(F^2 + x_1^2\right), \end{aligned} \tag{17}$$

where $D = m_d - k_{eff} + k_{dis}$.

The Fx_1 in (16) satisfies the inequality (18).

$$Fx_1 \le (F^2 + x_1^2)/2. \tag{18}$$

The inequality (19) is obtained by substituting (17) and (18) into (16).

$$\begin{aligned} \dot{V} \le -\frac{1}{2}Ax_2^2 - \left(-\frac{1+D^2}{2A} + C - \frac{1}{2}\right)x_1^2 \\ + \left(\frac{1+D^2}{2A} + \frac{1}{2}\right)F^2. \end{aligned} \tag{19}$$

Coefficients of $-x_2^2$, $-{x_1}^2$, and F^2 should be positive definite for the inequality (19) to satisfy the ISS conditions (9). Two additional conditions are required so that the coefficients of $-x_1^2$ and F^2 become positive definite.

$$\text{Condition III}: \; -\frac{1+D^2}{2A} + C - \frac{1}{2} > 0. \tag{20}$$

$$\text{Condition IV}: \frac{1+D^2}{2A} + \frac{1}{2} > 0. \tag{21}$$

Table 1 summarizes the four conditions for ISS. The conditions are expressed as the function of the physical properties of the device (m_d, b_d), k_{dis}, $\dot{k}_{dis}$, and T.

IV. CONTROL DESIGN FOR STABILIZATION

A. CONTROL DESIGN TO SATISFY ISS CONDITIONS

An ISS region that satisfies the four conditions in Table 1 is computed, and a controller for stabilizing the system is proposed in this section. The ISS region of the system (6) is shown in Fig. 4. The x and y axes represent k_{dis} and $\dot{k}_{dis}$, respectively. Condition I ($= k_{dis} + b_{eff} = \left(1 - \frac{T}{2}\right)k_{dis} + b_d$) is always positive definite when T is less than 2 s since k_{dis} and b_d are positive. The value of $A(= b_{eff} - m_d = b_d - \frac{T}{2}k_{dis} - m_d)$ corresponding to the condition II decreases

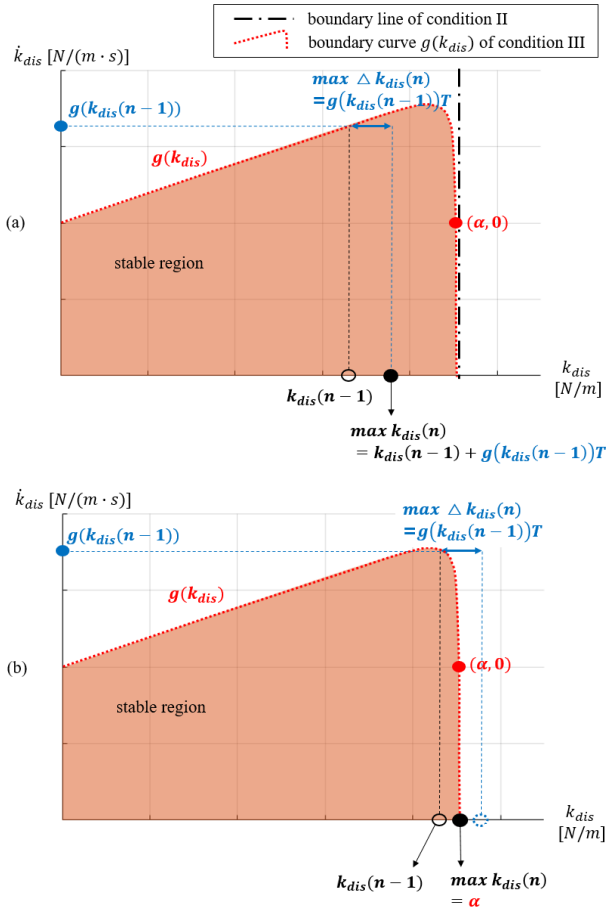

FIGURE 4. (a) $max\ k_{dis}(n)$ determined as $k_{dis}(n-1) + b(k_{dis}(n-1))T$; (b) $max\ k_{dis}(n)$ determined as α.

as k_{dis} increases. There is a constraint on the maximum k_{dis} by the condition II. Equation (22) represent the function of k_{dis} that satisfy the condition II. The $-\left(1 + D^2\right)/(2A)$ term in the condition III becomes a large negative value as the A approaches $+0$. An asymptotic line of condition III is the same as the boundary line of condition II as shown in Fig. 4 (a). Hence, condition III is more conservative than condition II. Equation (23) represent the function of k_{dis} and $\dot{k}_{dis}$ that satisfy the condition III. Equation (24) is a boundary curve $g(k_{dis})$ of the condition III (23), and it is represented in Fig. 4 (a). The $\left(1 + D^2\right)/(2A)$ term in the condition IV is positive definite if the A is positive definite. The condition IV is satisfied if the condition II is satisfied.

$$\text{Condition II}: k_{dis} < \frac{2}{T}(b_d - m_d). \tag{22}$$

Condition III:

$$\begin{aligned} -\frac{T^2}{4}\dot{k}_{dis}^2 + \left\{-m_dT - \left(\frac{T}{4} - \frac{1}{2}\right)\sigma\right\}\dot{k}_{dis} \\ + \left\{-b_d + m_d\left(1 - m_d\right) + k_{dis}\left(-\sigma + \frac{T}{2}\right) - 1\right\} > 0, \end{aligned} \tag{23}$$

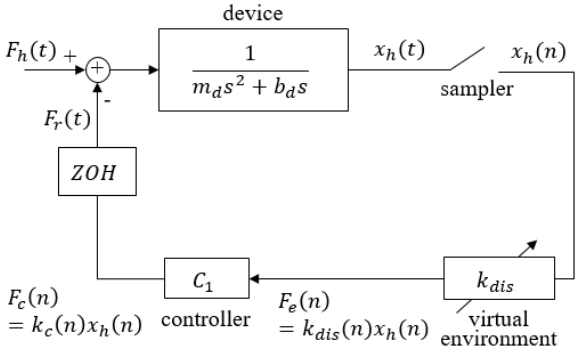

FIGURE 5. Haptic systems with the proposed controller C_1.

where $\sigma = 2(m_d - b_d) + k_{dis}T$.

$$g\left(k_{dis}\right) = \frac{k_{dis}\left(2T - T^2\right) + b_d\left(2T - 4\right) + m_d\left(4 - 6T\right) + \sigma_1}{2T^2}, \tag{24}$$

where the equation can be derived, as shown at the bottom of next page.

$\dot{k}_{dis}$ and k_{dis} cannot exceed the boundary curve $g(k_{dis})$ to satisfy the ISS conditions. Stability is guaranteed by limiting $\dot{k}_{dis}$ and k_{dis} to the $g(k_{dis})$. Value of $\dot{k}_{dis}$ is less than or equal to 0 N/(m·s) when the limit of maximum k_{dis} occurs. Equation (25) represents a maximum displayed stiffness α satisfying $g(k_{dis})$ when $\dot{k}_{dis}$ is 0 N/(m·s) as shown in Fig. 4 (a).

$$\alpha = \frac{4\left(b_d - m_d\right) + T + \sigma_2}{4T}, \tag{25}$$

where the equation can be derived, as shown at the bottom of next page.

A controller C_1 is proposed to adjust the change rate of k_{dis} to satisfy the ISS conditions in Fig. 4. $k_{dis}(n)$ is calculated as $F_e(n)$ divided by $x_h(n)$ in each time step when the contact occurs. $\dot{k}_{dis}(n)$ is calculated using backward Euler as in (26). The controller C_1 shown in Fig. 5 operates when contact occurs. $k_{dis}(n)$ is controlled to satisfy the conditions of $g(k_{dis})$ and α. $k_c(n)$ denotes the controlled $k_{dis}(n)$. The controlled force $F_c(n) = k_c(n)\,x_h(n)$ is transmitted to the operator.

$$\dot{k}_{dis}(n) = \frac{\Delta k_{dis}(n)}{T} = \frac{k_{dis}(n) - k_{dis}(n-1)}{T}. \tag{26}$$

The ISS conditions may not be satisfied when k_{dis} increases rapidly or k_{dis} is larger than α. The controller adjust the increase rate of k_{dis} to satisfy the ISS conditions, thereby $k_{dis}(n)$ is limited as $max\ k_{dis}(n)$. There are two $max\ k_{dis}(n)$ candidates to satisfy the ISS conditions. $max\ k_{dis}(n)$ candidate I and II are the conditions to satisfy $g(k_{dis})$ and α, respectively. Equation (27) shows $max\ k_{dis}(n)$ candidate I determined by $g(k_{dis})$. $max\ k_{dis}(n)$ in (27) is restricted as $g\left(k_{dis}(n-1)\right)T$ if the ISS conditions are not satisfied due to the large increase rate of k_{dis}. Equation (28) shows $max\ k_{dis}(n)$ candidate II determined as α. $k_{dis}(n)$ is limited as (28) if it is larger than α. $max\ k_{dis}(n)$ shown in (29) is selected as the value that satisfies both candidates (27), (28).

TABLE 2. $ZOH(z)\,sampler(z)$ using the continuous-to-discrete-time conversion.

Conversion method	$ZOH(z)sampler(z)$
Zero-order hold	$\frac{0.86}{z - 0.14}$
First-order hold	$\frac{0.57z + 0.30}{z - 0.13}$
Tustin approximation	$\frac{z+1}{2z}$
Impulse-invariant mapping	$\frac{2z}{z - 0.14}$
Zero-pole matching equivalents	$\frac{0.86}{z - 0.14}$

Fig. 4 (a) indicates a case in which $k_{dis}(n-1) + g\left(k_{dis}(n-1)\right)T$ is less than α. Hence $max\ k_{dis}(n)$ is chosen as $k_{dis}(n-1) + g\left(k_{dis}(n-1)\right)T$. Fig. 4 (b) shows a case in which $max\ k_{dis}(n)$ is determined as α since α is less than $k_{dis}(n-1) + g\left(k_{dis}(n-1)\right)T$.

$max\ k_{dis}(n)$ candidate I:

$$\begin{aligned} max\ k_{dis}(n) &= k_{dis}(n-1) + max\ \Delta\, k_{dis}(n) \\ &= k_{dis}(n-1) + g\left(k_{dis}(n-1)\right)T. \end{aligned} \tag{27}$$

$max\ k_{dis}(n)$ candidates II:

$$max\ k_{dis}(n) = \alpha. \tag{28}$$

$$max\ k_{dis}(n) = min\{k_{dis}(n-1) + g\left(k_{dis}(n-1)\right)T, \alpha\}. \tag{29}$$

$k_c(n)$ is bound to $max\ k_{dis}(n)$ as (30) if $k_{dis}(n)$ is larger than $max\ k_{dis}(n)$. In other cases, the measured $k_{dis}(n)$ is used as $k_c(n)$. The controlled force $F_c(n) = k_c(n)\,x_h(n)$ is rendered to the operator.

$$\begin{aligned} &\text{if } \left(k_{dis}(n) \geq \max\ k_{dis}(n)\right), \quad k_c(n) = max\ k_{dis}(n), \\ &\text{else} \quad k_c(n) = F_e(n)/x_h(n), \\ &F_c(n) = k_c(n)\,x_h(n). \end{aligned} \tag{30}$$

B. CONTROL DESIGN TO ENHANCE PERFORMANCE

The controller C_1 cannot render the stiffness of over α. This section presents an additional compensator for rendering of increased stiffness. The unintended damping, $-\frac{T}{2}k_{dis}(t)$ and spring, $-\frac{T}{2}\dot{k}_{dis}(t)$ occur due to the discretization effect caused by ZOH and sampler as in (6). The compensator is designed to reduce the discretization effect. The stability of the system with the compensator is analyzed based on the ISS conditions. A controller C_2 is proposed to satisfy the ISS conditions. The controller C_2 bounds the change rate of $k_{dis}(t)$, and there is no maximum stiffness constraint α that exists in the controller C_1.

$ZOH(s)\,sampler(s)$ in (2) is approximated using the first-order Padé approximation as shown in (31), and $ZOH(z)sampler(z)$ is calculated using continuous-to-discrete-time conversion. $C(z)$ is obtained by taking the inverse of $ZOH(z)sampler(z)$. Table 2 and Fig. 6 show

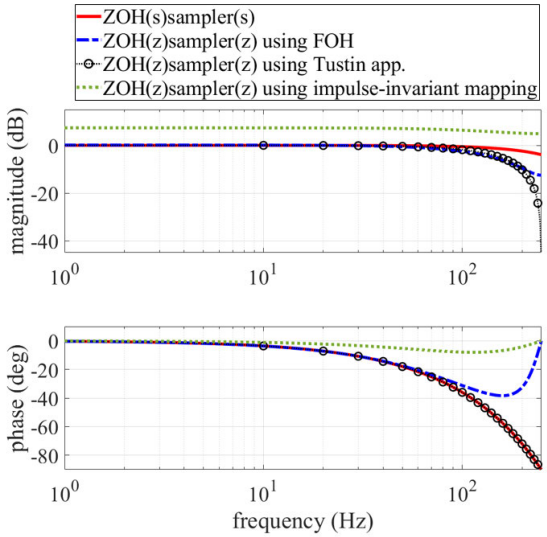

FIGURE 6. Bode plots of *ZOH* (*z*) *sampler*(*z*) using continuous-to-discrete-time conversion.

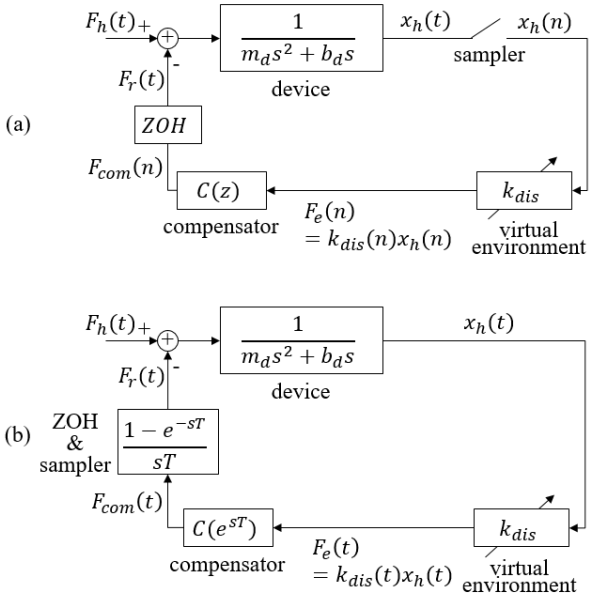

FIGURE 7. (a) Haptic systems with *C*(*z*); (b) Equivalence in the continuous-time domain.

$ZOH(z)sampler(z)$ using the continuous-to-discrete-time conversion methods when T is 2 ms. First-order hold (FOH), Tustin approximation, and impulse-invariant mapping are suitable among the conversion methods for $C(z)$ to become a causal compensator. The more magnitude and phase of $ZOH(z)\,sampler(z)$ is similar to that of $ZOH(s)\,sampler(s)$, the more discretization effect is effectively compensated. $ZOH(z)\,sampler(z)$ using impulse-invariant mapping has larger magnitude than $ZOH(s)\,sampler(s)$ and cannot express the phase lag of $ZOH(s)\,sampler(s)$. There is a limitation to improving the stability of the system since it cannot express the phase lag. $ZOH(z)\,sampler(z)$ using Tustin approximation accurately expresses the phase lag of $ZOH(s)\,sampler(s)$, but the magnitude becomes very small near the Nyquist frequency. Hence $C(z)$ using Tustin approximation amplifies high-frequency noise. $ZOH(z)\,sampler(z)$ using FOH has an error in the phase near the Nyquist frequency, but the phase is expressed accurately in the low-frequency region. The magnitude error near Nyquist frequency is smaller than that of $ZOH(z)\,sampler(z)$ using Tustin approximation. $ZOH(z)\,sampler(z)$ using FOH, therefore, is used for $C(z)$ as in (32).

$$ZOH(s)\,\widetilde{sampler}(s) = \frac{1}{\frac{T}{2}s+1}. \tag{31}$$

$$\begin{aligned} C(z) &= \frac{1}{ZOH(z)\,sampler(z)} \\ &= \frac{1}{\frac{(z-1)^2}{zT}Z\left\{\frac{ZOH(s)\widetilde{sampler}(s)}{s}\right\}} \\ &= \frac{z-0.13}{0.57z+0.30}. \end{aligned} \tag{32}$$

Fig. 7 (a) shows the haptic systems with $C(z)$. Fig. 7 (b) shows the equivalence in continuous time-domain. $ZOH(s)\,sampler(s)C(z)$ is defined as $H(s)$, and $H(s)$ is approximated to the first order term using Taylor series as in (33). It is known that the operator applies a position input of up to 20 Hz in haptic rendering [7]. The terms of the second or higher order in the Taylor series (33) are considered negligible considering the maximum frequency of 20 Hz is small compared to the sampling frequency, 500 Hz. Fig. 8 shows $ZOH(s)\,sampler(s)$, $ZOH(s)\,sampler(s)C(z)$ and the approximated $ZOH(s)\,sampler(s)C(z)$ in (33). It is shown that the approximated $ZOH(s)\,sampler(s)C(z)$ is identical with $ZOH(s)\,sampler(s)C(z)$ in the regions below 20 Hz. The phase lag occurring in the $ZOH(s)\,sampler(s)$ is

$$\sigma_1 = \sqrt{\left(T^4-20T^3+4T^2\right)k_{dis}^2+\{\left(-4T^3+48T^2-16T\right)b_d+(12T^3-64T^2+16T)m_d+8T^3\}k_{dis}+\{\left(4T^2-16T+16\right)b_d+(-24T^2+64T-32)m_d-16T^2\}b_d+\left\{\left(20T^2-48T+16\right)m_d+16T^2\right\}m_d-16T^2}$$

$$\sigma_2 = 2\sqrt{b_d\left(4b_d-8m_d-2T\right)+m_d\left(-4m_dT+4m_d+2T\right)+\frac{T^2}{4}-4T}$$

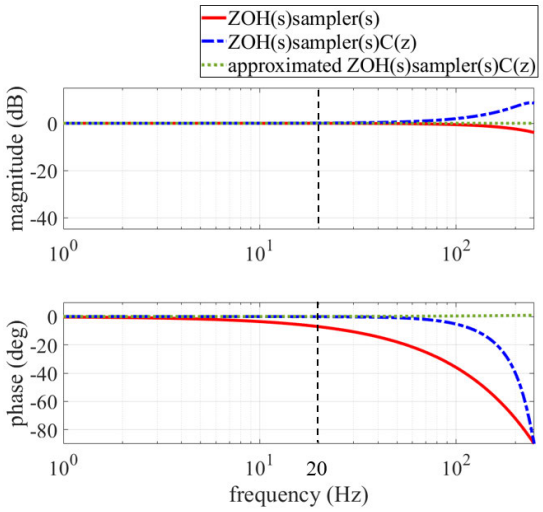

FIGURE 8. Bode plots of the approximated *ZOH* (*s*) *sampler* (*s*) *C* (*z*).

reduced by adding $C(z)$.

$$\begin{aligned} H\left(s\right) &= ZOH\left(s\right) sampler\left(s\right) C\left(z\right) \\ &= \left(\frac{1-e^{-sT}}{sT}\right)\left(\frac{e^{sT}-0.13}{0.57e^{sT}+0.30}\right) \\ &\cong 1+H'\left(0\right)s = 1+5\times10^{-3}Ts. \end{aligned} \tag{33}$$

Equation (34) shows the rendered force $F_r\left(t\right) = F_e\left(n\right) C\left(z\right) ZOH$ in the continuous-time domain. $F_e\left(t\right)$ is the environment force in the continuous-time domain as shown in Fig. 7 (b). $F_e\left(s\right)$ is Laplace transformation of $F_e\left(t\right)$. $F_e\left(t\right)$ is same as $k_{dis}\left(t\right) x_h\left(t\right)$. $F_e\left(n\right) C\left(z\right) ZOH$ is equivalent to the inverse Laplace transform of $F_e\left(s\right) C\left(e^{sT}\right) \frac{1-e^{-sT}}{sT}$ and approximated as the inverse Laplace transform of $F_e\left(s\right)\left(1+H'\left(0\right)s\right)$ using (33). Hence $F_r\left(t\right)$ is expressed as a function of $k_{dis}\left(t\right), x_h\left(t\right)$ and T. An ideal $F_r\left(t\right)$ is same as $k_{dis}\left(t\right) x_h\left(t\right)$. $F_r\left(t\right)$ under the $H\left(s\right)$ becomes $k_{dis}\left(t\right) x_h\left(t\right)$ with additional terms, $H'\left(0\right) k_{dis}\left(t\right) \dot{x_h}\left(t\right)$ and $H'\left(0\right) \dot{k}_{dis}\left(t\right) x_h\left(t\right)$ as in (34), resulting in unintended force of damping and springs.

$$\begin{aligned} F_r\left(t\right) &= F_e\left(n\right) C\left(z\right) ZOH \\ &= \mathcal{L}^{-1}\left\{F_e\left(s\right) C\left(e^{sT}\right) ZOH\left(s\right) sampler\left(s\right)\right\} \\ &\cong \mathcal{L}^{-1}\left\{F_e\left(s\right)\left(1+H'\left(0\right)s\right)\right\} \\ &= F_e\left(t\right) + H'\left(0\right)\frac{d}{dt}\left(F_e\left(t\right)\right) \\ &= \left\{k_{dis}\left(t\right) + H'\left(0\right)\dot{k}_{dis}\left(t\right)\right\} x_h\left(t\right) \\ &\quad + H'\left(0\right) k_{dis}\left(t\right) \dot{x_h}\left(t\right). \end{aligned} \tag{34}$$

Differential equation of the system is shown in (35). The unintended damping, $H'\left(0\right) k_{dis}\left(t\right)$ and spring, $H'\left(0\right) \dot{k}_{dis}\left(t\right)$ occur due to $H\left(s\right)$. Hence, the effective damping $b_{eff}\left(t\right)$ and spring $k_{eff}\left(t\right)$ of the system become $b_d + H'\left(0\right) k_{dis}\left(t\right)$ and $k_{dis}\left(t\right) + H'\left(0\right) \dot{k}_{dis}\left(t\right)$, respectively. The haptic system is expressed as the linear time-varying system where $b_{eff}\left(t\right)$ and $k_{eff}\left(t\right)$ vary according to $k_{dis}\left(t\right)$ and T. Table 3 shows the $b_{eff}\left(t\right)$ and $k_{eff}\left(t\right)$ of the system with and without $C\left(z\right)$. The

TABLE 3. $b_{eff}(t)$ and $k_{eff}(t)$ of the system with and without $C(z)$.

	w/o $C(z)$	w/ $C(z)$
$b_{eff}(t)$	$b_d - \frac{T}{2}k_{dis}(t)$	$b_d + 5\times10^{-3}Tk_{dis}(t)$
$k_{eff}(t)$	$k_{dis}(t) - \frac{T}{2}\dot{k}_{dis}(t)$	$k_{dis}(t) + 5\times10^{-3}T\dot{k}_{dis}(t)$

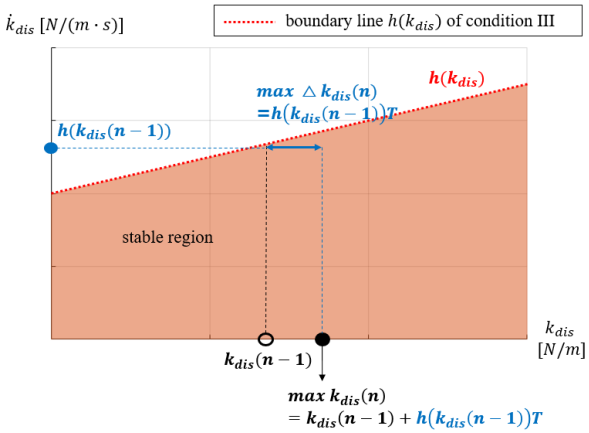

FIGURE 9. *max* $k_{dis}(n)$ to satisfy $h(k_{dis})$.

effect of negative damping and spring caused by ZOH and sampler is reduced by adding $C\left(z\right)$.

$$\begin{aligned} F_h\left(t\right) &= m_d\ddot{x_h}\left(t\right) + b_d\dot{x_h}\left(t\right) + F_r\left(t\right) \\ &\cong m_d\ddot{x_h}\left(t\right) + \left\{b_d + H'\left(0\right)k_{dis}\left(t\right)\right\}\dot{x_h}\left(t\right) \\ &\quad + \left\{k_{dis}\left(t\right) + H'\left(0\right)\dot{k}_{dis}\left(t\right)\right\} x_h\left(t\right) \\ &= m_d\left(t\right)\ddot{x_h}\left(t\right) + b_{eff}\left(t\right)\dot{x_h}\left(t\right) + k_{eff}\left(t\right) x_h\left(t\right), \end{aligned} \tag{35}$$

where $b_{eff}(t)$, $k_{eff}(t)$ and $H'\left(0\right)$ denote $b_d + H'\left(0\right) k_{dis}\left(t\right)$, $k_{dis}\left(t\right) + H'\left(0\right) \dot{k}_{dis}\left(t\right)$ and $5\times10^{-3}T$, respectively.

The ISS of the system with $C(z)$ is analyzed using the ISS-Lyapunov function candidate (10). The four conditions in Table 1 should be satisfied for the system (35) to be ISS. Fig. 9 shows the region that satisfies the four conditions according to k_{dis} and $\dot{k}_{dis}$. Condition I ($= k_{dis} + b_{eff} = \left(1+5\times10^{-3}T\right)k_{dis} + b_d$) is always positive definite since k_{dis} and b_d are positive. The value of $A(= b_{eff} - m_d = b_d + 5\times10^{-3}Tk_{dis} - m_d)$ corresponding to the condition II increases as k_{dis} increases. Hence, there is no constraint on the maximum displayed stiffness. The system without $C(z)$ has the constraint on the value of A as shown in (22). The system with $C(z)$ always satisfies the condition II by reducing the discretization effect, which improves the stable region. The $\left(1+D^2\right)/(2A)$ term in the condition IV is positive definite if the A is positive definite. The condition IV is satisfied if the condition II is satisfied. The system is, therefore, ISS if the condition III is satisfied. Equation (36) shows the function of the condition III. $\dot{k}_{dis}^2$ term in (36) is neglected since the coefficient of $\dot{k}_{dis}^2$ is very small as compared to other terms. The boundary line of (36) is defined as $h(k_{dis})$ and expressed in (37).

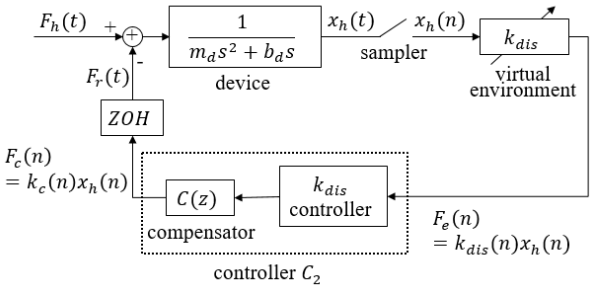

FIGURE 10. The controller C_2 for rendering of increased stiffness.

Condition III:

$$-\frac{T^2}{4\times 10^4}\dot{k}_{dis}^2+\left\{\frac{m_d T}{100}-\left(\frac{T}{400}+\frac{1}{2}\right)\sigma\right\}\dot{k}_{dis} + \left(m_d - b_d + k_{dis}\sigma - m_d^2 - \frac{k_{dis}T}{200} - 1\right) > 0, \quad (36)$$

where $\sigma = 2b_d - 2m_d + \frac{k_{dis}T}{100}$.

$$\dot{k}_{dis} < \frac{-m_d + b_d - k_{dis}\sigma + m_d^2 + \frac{k_{dis}T}{200} + 1}{\frac{m_d T}{100} - \left(\frac{T}{400}+\frac{1}{2}\right)\sigma} = h\left(k_{dis}\right), \quad (37)$$

where $\sigma = 2b_d - 2m_d + \frac{k_{dis}T}{100}$.

The stiffness change rate is constrained as $h(k_{dis})$ to satisfy the conditions. It is confirmed that the ISS region with $C(z)$ is expanded compared to the ISS region without $C(z)$ shown in Fig. 4. The maximum displayed stiffness of the system without $C(z)$ is limited to α as shown in Fig. 4, whereas there is no constraint on the maximum displayed stiffness of the system with $C(z)$.

A controller C_2 that satisfies the ISS conditions is proposed. $k_{dis}(n)$ is calculated as $F_e(n)$ divided by $x_h(n)$ in each time step when the contact occurs. $\dot{k}_{dis}(n)$ is calculated using backward Euler as in (26). The controller C_2 shown in Fig. 10 operates when contact occurs. $k_{dis}(n)$ is controlled to satisfy the conditions of $h(k_{dis})$. $k_c(n)$ denotes the controlled $k_{dis}(n)$. $max\ \Delta k_{dis}(n)$ in (38) is limited as $h\left(k_{dis}(n-1)\right)T$ if the conditions are not satisfied due to rapidly increasing of $k_{dis}(n)$. Fig. 9 shows how the controller operates. $k_c(n)$ is bound to $max\ k_{dis}(n)$ as in (39) if $k_{dis}(n)$ is larger than $max\ k_{dis}(n)$. In other cases, the measured $k_{dis}(n)$ is used as $k_c(n)$. The controlled force $F_c(n) = k_c(n)x_h(n)$ is rendered to the operator. The controller C_2 does not have the constraint on the maximum renderable stiffness α (28) that the controller C_1 has. Hence, the stiff environment can be rendered.

$$max\ k_{dis}(n) = k_{dis}(n-1) + h\left(k_{dis}(n-1)\right)T. \quad (38)$$

$$if\ \left(k_{dis}(n) \geq max\ k_{dis}(n)\right),\quad k_c(n) = max\ k_{dis}(n),$$
$$else\quad k_c(n) = F_e(n)/x_h(n),$$
$$F_c(n) = k_c(n)x_h(n). \quad (39)$$

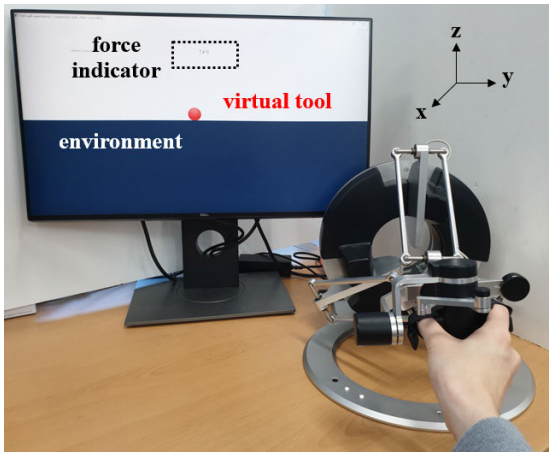

FIGURE 11. Experiment setup.

V. EXPERIMENTS

The ISS region is computed for an example using a commercial haptic device Omega 7 as shown in Fig. 11. The feasibility of the proposed method is confirmed by analyzing the ISS region of the system using Omega 7 in the 1-DOF of the z-direction, which is the direction of gravity. The proposed method can be extended straightforwardly to multi-DOF haptic rendering by defining k_{dis} in x, y, and z-directions, respectively.

The physical properties of the device with its local controller are measured to compute the ISS region. Force input of chirp signal that varies from 0.1 Hz to 30 Hz with an amplitude of 1.5 N is applied to the z-direction. The position of the end effector is measured from the encoder. The velocity and acceleration are calculated using a zero-phase filter. The properties in (40), mainly used for the model of the haptic device with its local controller [28], are optimized using the Levenberg-Marquardt algorithm. The device mass m_d, device damping b_d, and Coulomb friction f_c are 0.285 kg, 0.739 Ns/m, and 0.243 N, respectively. The relative percent difference error between the input force and the estimated force using the optimized properties is 13.91%.

$$F = m_d\ddot{x} + b_d\dot{x} - f_c sgn\left(\dot{x}\right). \quad (40)$$

The ISS region of the system without $C(z)$ in Section IV-A is computed. The four conditions in Table 1 are expressed as the function of device properties the haptic device such as mass m_d, damping b_d, stiffness k_{dis}, change rate of stiffness $\dot{k}_{dis}$, and sampling time T. Function value of each condition according to k_{dis} and $\dot{k}_{dis}$ is calculated by substituting the device properties, k_{dis}, $\dot{k}_{dis}$, and T into the function of the four conditions. Fig. 12 shows the region that satisfies each condition according to k_{dis} and $\dot{k}_{dis}$ when T is 2 ms. Colors of the graphs represent the function value of conditions that satisfy the ISS. The function value of each condition should be larger than zero to be ISS. Hence the value less than zero is not shown in the graph. Ranges of k_{dis} and $\dot{k}_{dis}$ are set to $0 \sim 600$ N/m and $-2000 \sim 2000$ N/(m·s), respectively. X and y-axis represent k_{dis} and $\dot{k}_{dis}$, respectively.

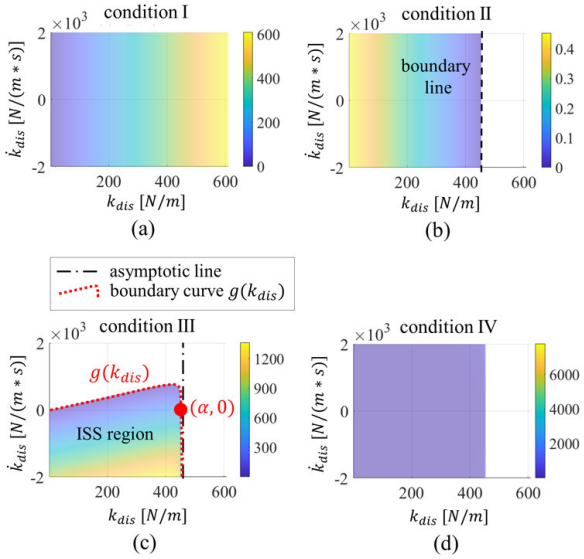

FIGURE 12. Four conditions for ISS of the system without $C(z)$.

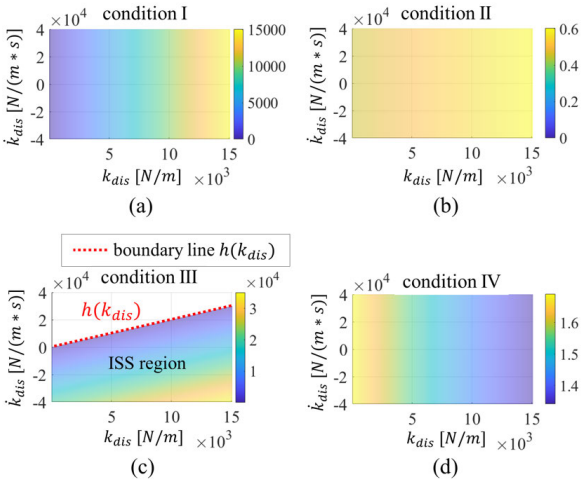

FIGURE 13. Four conditions for ISS of the system with $C(z)$.

Condition I is always positive definite regardless of k_{dis} and $\dot{k}_{dis}$. The black-dashed line shown in Fig. 12 (b) represents the boundary conditions of (22). An asymptotic line of condition III in Fig. 12 (c) is the same as the boundary line of condition II. The boundary curve $g(k_{dis})$ indicated by red dots in Fig. 12 (c) represent the boundary conditions of (23). The $\left(1+D^2\right)/(2A)$ term in the condition IV is positive definite if the A is positive definite. The condition IV is satisfied if the condition II is satisfied.

The ISS region that satisfies the all conditions is shown in Fig. 12 (c). Equation (41) represents the boundary curve $g(k_{dis})$. The maximum displayed stiffness α (25) is 453 N/m. The $g\left(k_{dis}\right)$ and α are used for the controller C_1 as in (27)-(30). The ISS region in Fig. 12 (c) shows that the ISS cannot be satisfied if the $\dot{k}_{dis}$ increases rapidly beyond the $g(k_{dis})$ or k_{dis} exceeds the maximum α (41), as shown at the bottom of the next page.

The ISS region of the system with $C(z)$ in Section IV-B is computed. The four conditions in Table 1 should be satisfied for the system (35) to be ISS. Fig. 13 shows the region that satisfies each stability condition according to k_{dis} and $\dot{k}_{dis}$ when T is 2 ms. Omega 7 can render a stiffness of up to 14.5 kN/m [29], hence the k_{dis} range is set taking this into account. Ranges of k_{dis} and $\dot{k}_{dis}$ are set to $0 \sim 15$ kN/m and $-40 \sim 40$ kN/(m·s), respectively. Colors of the graphs represent the function values of condition that satisfy the ISS. The function value of each condition should be larger than zero to be ISS. Hence the value less than zero is not shown in the graph. Condition I, II, IV are always positive definite regardless of k_{dis} and $\dot{k}_{dis}$. The system is ISS if the condition III is satisfied. The system without $C(z)$ has the constraint on the value of $A(=b_{eff}-m_d)$ corresponding to condition II as shown in Fig. 12 (b). The system with $C(z)$ always satisfies the condition II by reducing the discretization effect, which improves the stable region. Equation (42) shows the function of the boundary line $h\left(k_{dis}\right)$ of condition III shown in Fig. 13 (c).

$$h\left(k_{dis}\right)=\frac{2.00\times10^5k_{dis}^2+9.07\times10^9k_{dis}+1.54\times10^{10}}{1.00\times10^5k_{dis}+4.54\times10^9}. \tag{42}$$

The ISS region of the system with $C(z)$ that satisfies all conditions is shown in Fig. 13 (c). It shows that the condition is always satisfied when the stiffness change rate is negative. The stiffness increase rate is constrained as $h(k_{dis})$ to satisfy the condition. It is confirmed that the ISS region with $C(z)$ is expanded compared to the ISS region without $C(z)$ shown in Fig. 12 (c). The $h(k_{dis})$ is used for the controller C_2 as in (38), (39).

Performance of the proposed controller C_1 and C_2 is experimentally compared with the virtual coupling and the FBA method, which are widely used passivity-based approaches. Fig. 11 shows the experiment setup using Omega 7. The experiments are conducted for 1-DOF in the z-direction. There is the virtual environment at a position less than 0 mm in the z-axis direction. The operator moves the device in the z-direction and contacts the environment. Experiments are performed in which the operator maintains a force of 10 N while looking at an indicator of the environment force. T is set to 2 ms, and b_d is 0.739 Ns/m as in (40). A spring of the virtual coupling k_{vc} is designed to satisfy Colgate's passivity condition [13] as in (43). A damping of the virtual coupling b_{vc} is set as 0 Ns/m to use the largest k_{vc}. The maximum stiffness k_{vc} that satisfy (43) is 739 N/m. Hence k_{vc} is set as 735 N/m. The FBA method considering the memory effect [9] is used in the experiments.

$$k_{vc}<\frac{2(b_d-|b_{vc}|)}{T}. \tag{43}$$

The virtual environment of the experiment is composed of the Hunt-Crossly model as in (44) that is widely used for nonlinear contact model [30]. k_e, b_e, and n are set as 5000, 100, and 1.5, respectively. The k_{dis} of the Hunt-Crossly model increases as the insertion depth increases. Soft properties are rendered at the beginning of the contact, and stiff properties

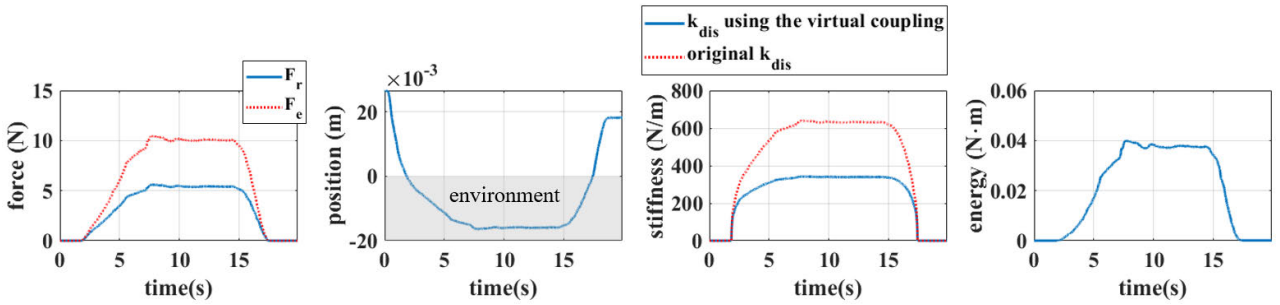

FIGURE 14. Experiment results using the virtual coupling.

TABLE 4. Error of rendered force in the experiment and the stored energy.

	RMSE	Maximum error	Stored energy
Virtual coupling	3.26 N	4.88 N	9.59×10^{-5} N · m
FBA	3.02 N	4.79 N	1.09×10^{-4} N · m
Controller C_1	1.95 N	3.03 N	-6.72×10^{-3} N · m
Controller C_2	0.43 N	2.40 N	-8.20×10^{-3} N · m

are rendered as the insertion depth increases.

$$F_e = k_e x^n + b_e x^n v. \tag{44}$$

Fig. 14 shows the experiment results using the virtual coupling. Smaller force is rendered compared to the environment force. The operator always feels stiffness softer than correct one when using the virtual coupling, since $k_{vc}(= 735N/m)$ is connected serially between the virtual tool and the haptic device. As an example, the original k_{dis} at 2.5 s and 6.4 s is 300 N/m and 600 N/m, respectively. The k_{dis} using the virtual coupling at this time is 213.3 N/m ($= 1/(1/300 + 1/k_{vc})$) and 330.3 N/m ($= 1/(1/600 + 1/k_{vc})$), respectively. The original k_{dis} increases as the insertion depth increase in the Hunt-crossly model. The error of the rendered force increases as the original k_{dis} increases. Energy stored in the system using (7) after the experiment is 9.59×10^{-5}N · m. Hence the generated energy is less than zero since the virtual coupling is designed to satisfy the passivity. Table 4 shows the error between the rendered force and the environment force. A root-mean-square error (RMSE) is 3.26 N, and a maximum error is 4.88 N.

Fig. 15 shows the experiment result using the FBA method considering the memory effect [9]. The computed environment force exceeds the passivity condition as the original k_{dis} increases. Force bounding does not occur at the initial contact, and soft properties are transmitted. Force bounding occurs when the insertion depth increases, and stiffer properties are transmitted. The rendered force is bounded at 4.608 s $\sim$ 17.096 s. The magnitude of the bounded force is less than 5.832 N. RMSE is 3.02 N, and a maximum error is 4.79 N. The environment force is transmitted faithfully if it is less than the computed maximum force. Energy stored in the system using (7) after the experiment is 1.09×10^{-4}N · m. Hence the generated energy is less than zero since the FBA method limits the maximum force to make the system passive.

Fig. 16 shows the experiment result using the proposed controller C_1. k_{dis} is controlled to gradually increase to satisfy the condition of $g(k_{dis})$ (27) at 1.188 s $\sim$ 2.910 s indicated by the dotted ellipse on the stiffness graph. k_{dis} exceeds α (28) at 3.472 s $\sim$ 17.224 s, thereby k_{dis} is limited to α. RMSE and maximum errors are 1.95 N and 3.03 N, respectively. RMSE and maximum errors using the controller C_1 are reduced by at least 35 % compared to using the virtual coupling and FBA method. Energy stored in the system using (7) after the experiment is -6.72×10^{-3}N · m. It means that the energy generated from the haptic system is a positive finite value. More energy is transferred to the operator compared to the passivity-based methods. The increased stiffness corresponding to the additionally transferred energy is rendered compared to the passivity-based method. Performance of haptic rendering is, therefore, improved. Soft tissue models used in medical simulations generally have a stiffness up to 400 N/m [31], [32]. The proposed controller C_1 is sufficient to render the haptic feedback of soft tissue since α is 453 N/m when T is 2 ms. There is, however, a limit to provide high fidelity haptic feedback when rendering the stiff environment with stiffness of more than 453 N/m.

Fig. 17 shows the results of the proposed controller C_2. $\dot{k}_{dis}$ is adjusted when k_{dis} increase rapidly in 1.064 s $\sim$ 2.464 s that is indicated by the dotted ellipse on the stiffness graph. k_{dis} is controlled to gradually increase to satisfy the condition of $h(k_{dis})$. An error of the rendered force occurs in this region. The environment force is faithfully rendered to the operator after k_c reaches the original k_{dis}. The RMSE and maximum errors are 0.43 N and 2.40 N, respectively. The error of the rendered force is summarized in Table 4. The RMSE and

$$g(k_{dis}) = 499.50k_{dis} - 2.2705 \times 10^5 + \sqrt{2.4750 \times 10^5 k_{dis}^2 - 2.2592 \times 10^8 k_{dis} + 5.1554 \times 10^{10}} \tag{41}$$

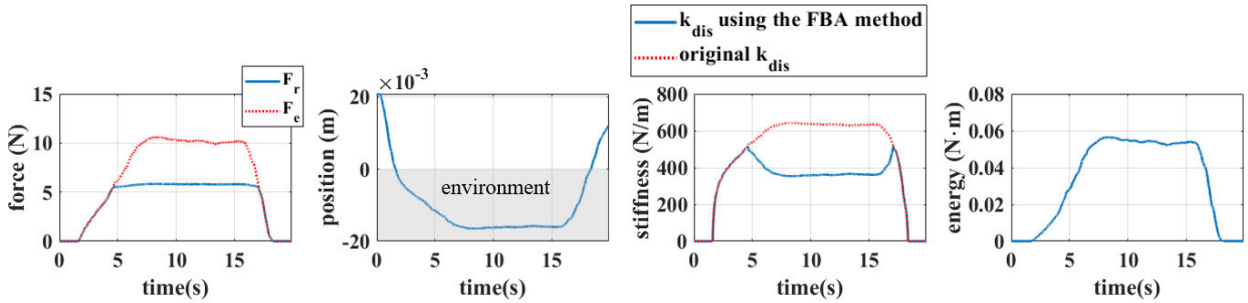

FIGURE 15. Experiment results using the FBA method.

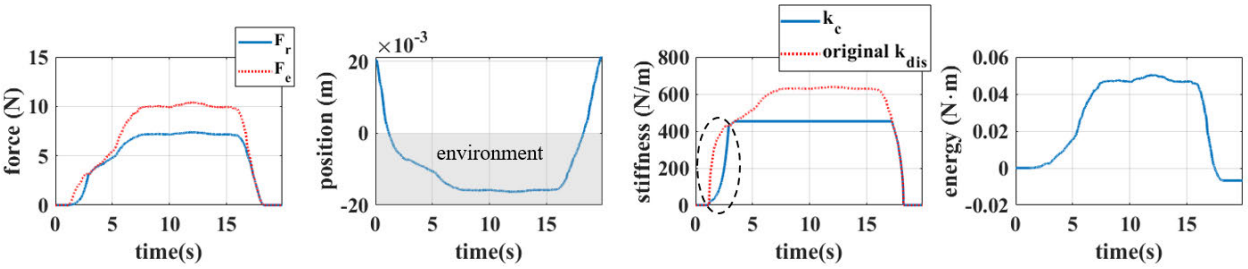

FIGURE 16. Experiment using the proposed controller C_1.

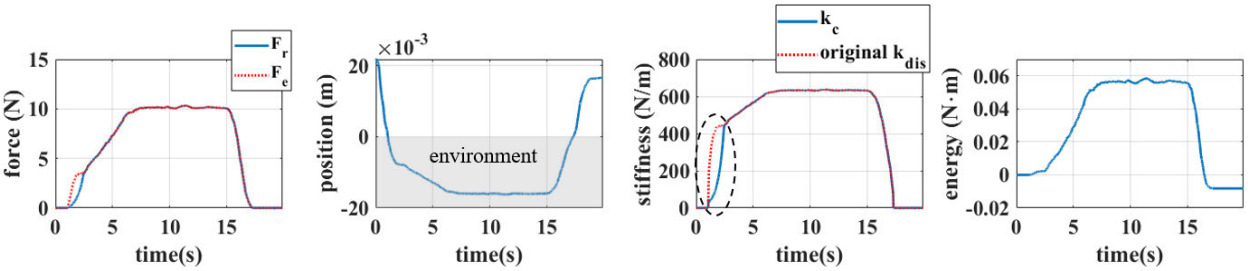

FIGURE 17. Experiment using the proposed controller C_2.

maximum error are reduced by at least 85.76 % and 49.90 %, respectively, compared to using virtual coupling and FBA method. The RMSE and maximum error are reduced by 77.95 % and 20.79 %, respectively, compared to using the controller C_1. Stored Energy in the system using (7) after the experiment is -8.20×10^{-3}N · m. The energy generated in the system is increased compared to the system with controller C_1 and passivity-based methods. This means that more energy is transferred to the operator, and the increased stiffness corresponding to the additionally transferred energy is rendered. Hence, the performance of haptic rendering is improved.

VI. CONCLUSION

This paper presents the control method to adjust the change rate of the environment stiffness based on the ISS conditions without the accurate model of the environment. The haptic systems become dissipative if they satisfy the ISS conditions. The generated surplus energy of the dissipative system may have a positive finite value. The proposed ISS-based control keeps the system dissipative, and the rendered force is controlled so that the generated energy has a positive finite value. More surplus energy of the dissipative system, compared to the passive system, can be transmitted to the operator. Hence increased stiffness of the environment corresponding to the surplus energy can be rendered to the operator, increasing the fidelity of the haptic system. The environment is modeled as the linear time-varying spring k_{dis}, and effective mass, spring, and damper of the system are analyzed in the continuous-time domain. The ISS conditions are analyzed, and the controller C_1 is proposed to satisfy the conditions. The controller C_2 is designed to enhance the performance using the compensator and ISS conditions. The compensator reduces negative damping and spring caused by the discretization effect, resulting in the wider ISS region. The k_{dis} is controlled to increase gradually to satisfy the ISS conditions if k_{dis} increases rapidly and deviates from the conditions. The environment force is faithfully rendered to the operator when the controlled k_{dis} reaches the original k_{dis}. The proposed controller uses only the current magnitudes of the device position and the environment force. The controller does not require any exact model of the environment. Hence, the proposed method guarantees the system stability with an unknown nonlinear environment. Experiment results show that the energy generated from the haptic system using the proposed method is a positive finite whereas the generated

energy using the passivity-based approaches is less than zero. This means that more energy is transferred to the operator compared to the passivity-based method. The proposed controller reduces the RMSE and maximum error by at least 85.76 % and 49.90 %, respectively, compared to using the virtual coupling or FBA methods.

REFERENCES

[1] D. Cleveland and K. Hashtrudi-Zaad, "The effect of discretization techniques on uncoupled stability of haptic simulation systems," in *Proc. IEEE Haptics Symp. (HAPTICS)*, Mar. 2018, pp. 66–71.
[2] V. Chawda, O. Celik, and M. K. O'Malley, "Evaluation of velocity estimation methods based on their effect on haptic device performance," *IEEE/ASME Trans. Mechatronics*, vol. 23, no. 2, pp. 604–613, Apr. 2018.
[3] T.-N. Nguyen, M.-C. H. B. Tho, and T.-T. Dao, "A systematic review of real-time medical simulations with soft-tissue deformation: Computational approaches, interaction devices, system architectures, and clinical validations," *Appl. Bionics Biomech.*, vol. 2020, pp. 1–30, Feb. 2020.
[4] B. Hannaford and J.-H. Ryu, "Time-domain passivity control of haptic interfaces," *IEEE Trans. Robot. Autom.*, vol. 18, no. 1, pp. 1–10, Feb. 2002.
[5] X. Xu, C. Schuwerk, B. Cizmeci, and E. Steinbach, "Energy prediction for teleoperation systems that combine the time domain passivity approach with perceptual deadband-based haptic data reduction," *IEEE Trans. Haptics*, vol. 9, no. 4, pp. 560–573, Oct. 2016.
[6] I. Desai, A. Gupta, and D. Chakraborty, "Rendering stiff virtual walls using model matching based haptic controller," *IEEE Trans. Haptics*, vol. 12, no. 2, pp. 166–178, Apr. 2019.
[7] D. Ryu, J. B. Song, S. Kang, and M. Kim, "Frequency domain stability observer and active damping control for stable haptic interaction," *IET Control Theory Appl.*, vol. 2, no. 4, pp. 261–268, Apr. 2008.
[8] K. Lee and D. Y. Lee, "Adjusting output-limiter for stable haptic rendering in virtual environments," *IEEE Trans. Control Syst. Technol.*, vol. 17, no. 4, pp. 768–779, Jul. 2009.
[9] J. P. Kim, S. Y. Baek, and J. Ryu, "A force bounding approach for multi-degree-of-freedom haptic interaction," *IEEE/ASME Trans. Mechatronics*, vol. 20, no. 3, pp. 1193–1203, Jun. 2015.
[10] S.-Y. Baek, S. Park, and J. Ryu, "An enhanced force bounding approach for stable haptic interaction by including friction," *Int. J. Precis. Eng. Manuf.*, vol. 18, no. 6, pp. 813–824, Jun. 2017.
[11] S.-Y. Baek, S. Park, and J. Ryu, "A force bounding approach in joint space for interacting with dynamic multi-degrees of freedom virtual objects," *IEEE Trans. Haptics*, vol. 12, no. 2, pp. 217–223, Apr. 2019.
[12] J. E. Colgate, M. C. Stanley, and J. M. Brown, "Issues in the haptic display of tool use," in *Proc. IEEE/RSJ Int. Conf. Intell. Robots Syst. Hum. Robot Interact. Cooperat. Robots*, vol. 3, Aug. 1995, pp. 140–145.
[13] J. E. Colgate and G. Schenkel, "Passivity of a class of sample data systems: Application to haptic interfaces," *J. Robot. Syst.*, vol. 14, no. 1, pp. 37–47, 1997.
[14] M. Kim and D. Lee, "Improving transparency of virtual coupling for haptic interaction with human force observer," *Robotica*, vol. 35, no. 2, pp. 354–369, Feb. 2017.
[15] H. Ding, H. Mitake, and S. Hasegawa, "Continuous collision detection for virtual proxy haptic rendering of deformable triangular mesh models," *IEEE Trans. Haptics*, vol. 12, no. 4, pp. 624–634, Oct. 2019.
[16] H. Ding and S. Hasegawa, "A 6-DoF zero-order dynamic deformable tool for haptic interactions of deformable and dynamic objects," in *Proc. Int. Conf. Hum. Haptic Sens. Touch Enabled Comput. Appl.*, 2020, pp. 244–252.
[17] C. Schuwerk, X. Xu, and E. Steinbach, "On the transparency of client/server-based haptic interaction with deformable objects," *IEEE Trans. Haptics*, vol. 10, no. 2, pp. 240–253, Apr. 2017.
[18] A. Jafari, M. Nabeel, and J.-H. Ryu, "The input-to-state stable (ISS) approach for stabilizing haptic interaction with virtual environments," *IEEE Trans. Robot.*, vol. 33, no. 4, pp. 948–963, Aug. 2017.
[19] M. Nabeel, A. Jafari, and J.-H. Ryu, "Realizing low-impedance rendering in admittance-type haptic interfaces using the input-to-state stable approach," in *Proc. IEEE/RSJ Int. Conf. Intell. Robots Syst. (IROS)*, Sep. 2017, pp. 914–919.
[20] A. Jafari and J.-H. Ryu, "Input-to-state stable approach to release the conservatism of passivity-based stable haptic interaction," in *Proc. IEEE Int. Conf. Robot. Automat. (ICRA)*, May 2015, pp. 285–290.
[21] N. Sivashankar and P. P. Khargonekar, "Robust stability and performance analysis of sampled-data systems," in *Proc. Amer. Control Conf. (ACC)*, 1998, pp. 1904–1908.
[22] H. Singh, A. Jafari, and J.-H. Ryu, "Increasing the rate-hardness of haptic interaction: Successive force augmentation approach," in *Proc. IEEE World Haptics Conf. (WHC)*, Jun. 2017, pp. 653–658.
[23] H. Singh, D. Janetzko, A. Jafari, B. Weber, C.-I. Lee, and J.-H. Ryu, "Enhancing the rate-hardness of haptic interaction: Successive force augmentation approach," *IEEE Trans. Ind. Electron.*, vol. 67, no. 1, pp. 809–819, Jan. 2020.
[24] E. D. Sontag, "Input to state stability: Basic concepts and results," in *Nonlinear and Optimal Control Theory*. Berlin, Germany: Springer, 2008, pp. 163–220.
[25] H. Li, L. Zhang, and K. Kawashima, "Operator dynamics for stability condition in haptic and teleoperation system: A survey," *Int. J. Med. Robot. Comput. Assist. Surg.*, vol. 14, no. 2, pp. 1–10, 2018.
[26] A. Mashayekhi, S. Behbahani, F. Ficuciello, and B. Siciliano, "Influence of human operator on stability of haptic rendering: A closed-form equation," *Int. J. Intell. Robot. Appl.*, vol. 4, no. 4, pp. 403–415, Dec. 2020.
[27] L. Tan and J. Jiang, *Digital Signal Processing: Fundamentals and Applications*, 3rd ed. New York, NY, USA: Academic, 2018.
[28] N. Colonnese and A. Okamura, "Stability and quantization-error analysis of haptic rendering of virtual stiffness and damping," *Int. J. Robot. Res.*, vol. 35, no. 9, pp. 1103–1120, Aug. 2016.
[29] Force Dimension. (2010). *Omega.7 Haptic Device*. [Online]. Available: http://www.forcedimension.com/downloads/specs/specsheet-omega.7.pdf
[30] R. Schindeler and K. Hashtrudi-Zaad, "Online identification of environment Hunt–Crossley models using polynomial linearization," *IEEE Trans. Robot.*, vol. 34, no. 2, pp. 447–458, Apr. 2018.
[31] A. Fouly, M. N. A. Nasr, A. M. R. F. E. Bab, and A. A. Abouelsoud, "Design, modeling and simulation of a micro tactile sensor for soft tissue stiffness measurement with three tips configuration," in *Proc. 7th Int. Conf. Comput. Intell., Model. Simul. (CIMSim)*, Jul. 2015, pp. 155–160.
[32] J. Zhang, Y. Zhong, and C. Gu, "Neural network modelling of soft tissue deformation for surgical simulation," *Artif. Intell. Med.*, vol. 97, pp. 61–70, Jun. 2019.

SUYONG KIM received the B.S., M.S., and Ph.D. degrees from the Department of Mechanical Engineering, Korea Advanced Institute of Science and Technology (KAIST), Daejeon, South Korea, in 2015, 2017, and 2022, respectively. He is currently a Postdoctoral Researcher with the KAIST. His research interests include medical robotics, control, and haptics.

DOO YONG LEE (Senior Member, IEEE) received the B.S. degree from the Department of Control and Instrumentation Engineering, Seoul National University, South Korea, in 1985, and the M.S. and Ph.D. degrees from the Department of Electrical, Computer, and Systems Engineering, Rensselaer Polytechnic Institute, Troy, NY, USA, in 1987 and 1993, respectively. From 1993 to 1994, he was a Postdoctoral Research Associate with the Rensselaer Polytechnic Institute. He joined the Department of Mechanical Engineering, Korea Advanced Institute of Science and Technology (KAIST), in 1994. He was the Director of Health Technology Infrastructure with the Korea Health Industry Development Institute, from 2010 to 2012, and the Head of the Department of Mechanical Engineering, KAIST, from 2017 to 2021. He was the President of the Institute of Control, Robotics, and Systems, in 2021. He is currently the POSCO Endowed Chair Professor of the KAIST. His research interests include robotics and simulation with medical applications, especially robotic medical devices, and high-fidelity interactive medical simulation with haptic interface for training and planning purposes. He is a member of the National Academy of Engineering of Korea. He received the Korea Prime Minister's Commendation in 2018 for technical contributions to the field.